pH-Gated Porosity Transitions of Polyelectrolyte Multilayers in Confined Geometries and Their Application as Tunable Bragg Reflectors

Lei Zhai,[‡] Adam J. Nolte,[‡] Robert E. Cohen,*[,†] and Michael F. Rubner*[,‡]

Department of Chemical Engineering and of Materials Science and Engineering, Massachusetts Institute of Technology, Cambridge, Massachusetts 02139

Received March 1, 2004; Revised Manuscript Received June 2, 2004

ABSTRACT: Polyelectrolyte multilayers with alternating porous and fully dense regions have been assembled from poly(acrylic acid) (PAA), poly(allylamine hydrochloride) (PAH), and poly(sodium 4-styrenesulfonate) (SPS) in appropriate combinations. The porous zones were developed postassembly via immersion of the heterostructure film into an aqueous acidic medium followed by rinsing in deionized water. Properly assembled PAH/PAA regions exhibit a reversible, pH-gated nanoporosity transition while PAH/SPS regions remain unchanged upon treatment at low pH. The application of these structures as one-dimensional dielectric mirrors and vapor sensors has been investigated. Organic liquid crystal molecules were also successfully loaded selectively into the nanoporous regions via a capillary force driven wicking action. Potential applications for drug delivery and as Bragg stacks with tunable refractive index layers are also discussed.

Introduction

Nano- and microporous polymers are useful in many applications including separation technologies,[1−4] catalyst surfaces and supports,[5−10] antireflection coatings,[11,12] drug delivery systems,[13−15] tissue engineering,[16−18] and templates for the growth of various nanoscopic materials.[19−22] Porous polymer systems have been prepared by a number of different techniques such as phase separation,[23−25] the selective dissolution of polymer blends,[11] the degradation of block copolymers,[26−28] and the polymerization of monomers in sacrificial colloidal[29−32] or nanoporous silica templates.[33] The ability to introduce nanoporosity selectively within specific regions of a polymer[27] has further extended the utility of these materials as photonic structures and as optical sensors.[33] Li et al.,[33] for example, reported the fabrication of a photonic polymeric assembly with alternating porous and solid regions by using porous silicon as a template for polymer infiltration. The use of these novel structures as vapor sensors, optical filters, and drug releasing materials was also demonstrated. Research in this area, however, has exposed the significant difficulties associated with controlling, at suitable length scales, the thickness, pore size, and level of porosity of spatially distinct regions within a solid polymer matrix. This is particularly true if one desires to fabricate heterostructures with a more complex arrangement of nanoporous regions such as would be needed to fabricate a Fabry−Perot microcavity.[34] As will be demonstrated in this work, the layer-by-layer processing schemes developed for the construction of polyelectrolyte multilayer films are ideally suited for this task.

Techniques to introduce microporosity in polyelectrolyte multilayers based on a low-pH solution treatment were first suggested by Mendelsohn et al.[35] Since then, a number of other strategies have been developed for creating both micro- and nanoporous multilayer films.[12,36−38] In our work, we have demonstrated that certain multilayer assemblies based on the weak polyelectrolytes poly(acrylic acid) (PAA) and poly(allylamine hydrochloride) (PAH) undergo a phase separation process at low pH that produces either micro- or nanoporous material depending on the treatment conditions.[12,35] In addition, these transitions to the porous state could be completely and repeatably reversed by treatment at a high pH. A pH-gated change in the degree of ionization of the PAA chains was the key element driving these transitions.

Building on this previous work, we now show that it is possible to fabricate polyelectrolyte multilayer heterostructures comprised of multiple nanoporous and solid regions. The spatial arrangement and thickness of different regions can be easily controlled at the molecular level through the layer-by-layer dipping process.[39] It will also be demonstrated that the nanopores can be opened and closed by using simple pH treatments. Thus, a key conclusion of this work is that reversible pH-gated nanoporosity transitions can be induced in PAH/PAA multilayers that are confined within and isolated by a nonporosity forming multilayer system. Finally, it will be demonstrated that the nanopores of these complex thin film heterostructures can be filled with nonionic small molecules through a simple infiltration process. Potential applications of these structures include tunable dielectric mirrors (Bragg reflectors), pH-gated dielectric mirrors, vapor sensors, and monitorable drug delivery systems.

Experimental Section

PAH (M_w = 70 000) and SPS (M_w = 70 000) were obtained from Sigma-Aldrich (St. Louis, MO). PAA (M_w = 90 000) was obtained from Polysciences (Warrington, PA). All the chemicals were used as received. Deionized water (>18 MΩ cm, Millipore Milli-Q), with an unadjusted pH of approximately 5.5, was exclusively used in all aqueous solutions and rinsing procedures. Liquid crystal E7 (a eutectic mixture of 4-cyano-4′-*n*-alkylbiphenyls) was purchased from EM Industries, Inc.

Polyelectrolyte multilayers (PEMs) were assembled on glass microscope slides, (3-aminopropyl)triethoxysilane-coated mi-

* To whom correspondence may be addressed. E-mail: R.E.C., recohen@mit.edu; M.F.R., rubner@mit.edu.
[†] Department of Chemical Engineering.
[‡] Department of Materials Science and Engineering.

10.1021/ma049593e CCC: $27.50
Published on Web 07/13/2004

croscope slides (LabScientific, Inc.), or polished single-crystal silicon wafers (⟨100⟩) using an automated Zeiss HMS slide stainer as previously described.[40] Silicon wafers and glass substrates were degreased in a detergent solution followed by deionized water rinses prior to multilayer assembly. Silane-coated microscope slides were used as received.

PAH/PAA blocks were built using pH 8.5 (±0.01) PAH (10^{-2} M by repeat unit) and pH 3.5 (±0.01) PAA (10^{-2} M) aqueous solutions which were pH adjusted by using either 1 M NaOH or 1 M HCl. PEMs on glass slides and silicon wafers were formed by first immersing substrates into the PAH solution for 15 min followed by one 2 min and two 1 min immersions into water as rinsing steps. Then, the substrates were immersed into the PAA solution for 15 min followed by identical rinsing steps. The adsorption and rinsing steps were repeated until the desired number of bilayers was obtained. One bilayer is defined as a single adsorption of a polycation followed by an adsorption of a polyanion; thus, a half-integer number of bilayers of PAH/PAA ends with PAH as the outermost layer.

PAH/SPS blocks were built on silane-coated substrates or on the top of PAH/PAA blocks using pH 4.0 (±0.01) SPS (10^{-2} M) and pH 4.0 (±0.01) PAH (10^{-2} M by repeat unit) aqueous solutions. NaCl was added to the SPS and PAH solutions to make 0.1 M NaCl solutions prior to pH adjustment. PEMs were formed by first immersing substrates into the SPS solution for 5 min followed by one 2 min and two 1 min immersions into water as rinsing steps. The substrates then were immersed into the PAH solution for 5 min followed by identical rinsing steps. The adsorption and rinsing steps were repeated until desired numbers of bilayers were obtained.

The thickness of dense films and films containing only two blocks was measured using ellipsometry (Gaertner) at wavelengths of 633 nm and profilometry (Tencor P10). The data obtained from these two methods are in good agreement (<10% difference). The thickness of films containing more than two blocks was measured using profilometry only since it is difficult to extract thickness values from multiblock structures using ellipsometry. All data sets in this paper represent at least two independent experiments. In all cases, the deviation between independent measurements was less than 10%. AFM characterization (Digital Instruments Dimension 3000 scanning probe microscope) was performed in tapping mode with Si cantilevers. Near-normal reflectivity (fixed 7° off normal to the plane of the film) from one side of a substrate was measured on a Cary 5E ultraviolet/visible/near-infrared spectrophotometer. The film on the other side of the substrate was removed and replaced with a black backing material.

The refractive index of the porous PAH/PAA blocks with air- or liquid-filled pores was estimated using an effective medium approximation.[41,42]

$$n_f = V_p n_l + (1 - V_p) n_s \quad (1)$$

$$V_p = (H - H_0)/H \quad (2)$$

In eq 1, n_f is the effective value of the refractive index for the air- or liquid-filled, porous PAH/PAA blocks, n_l is the known refractive index of air or the infiltrated liquid, and n_s is the refractive index of a fully dense PAH/PAA block. V_p is the pore fraction of the porous PAH/PAA block. H_0 and H are the block thickness before and after porosity transitions. This approximation was used to obtain an effective refractive index of the PAH/PAA blocks in Bragg reflectors and vapor sensors. Index values calculated this way compare favorably to those obtained by means of simulation (within 5% or better).

Theoretical reflectivity responses (simulations) were calculated using the transfer matrix method attributed to Abeles.[43] To produce the theoretical spectral responses in this paper, the matrix method was implemented in MATLAB. As described by Hecht,[44] the thicknesses and refractive index data were used to create a unique 2 by 2 matrix for each region in the structure. These 2 by 2 matrices were subsequently multiplied together in the order they appeared to create a total transfer matrix for the entire structure. A straightforward equation[44] was then used to derive theoretical reflectance values from the entries of the total transfer matrix. Because the entries of each matrix were dependent upon the wavelength of the incident light, the above procedure was repeated multiple times over a range of wavelengths to give theoretical reflectance vs wavelength plots.

Simulating the optical response of a Bragg reflector requires knowing the thickness and refractive index of each region in the structure. According to Bragg's law, the first-order reflected wavelength of a structure with a periodic index profile is given as[45]

$$\lambda_1 = 2(n_p d_p + n_{np} d_{np}) \quad (3)$$

where λ_1 is the first-order reflected wavelength and n_p, d_p, n_{np}, and d_{np} are the refractive indices and thicknesses of the porous PAH/PAA and nonporous PAH/SPS regions, respectively. The refractive index of the porous PAH/PAA blocks (n_p) can be calculated if the remaining variables in eq 3 are known. The thickness values for the individual dense PAH/PAA and PAH/SPS regions were obtained by measuring the thickness of a film after the addition of each block. The average thickness value of the PAH/SPS regions was used for d_{np}. After the porosity treatment, the average thickness of the porous PAH/PAA regions, d_p, was obtained by subtracting the thicknesses of the PAH/SPS regions, which did not change during the treatment,[46] from the total thickness of treated films according to eq 4:

$$d_p = (d_t - N_{np} d_{np})/N_p \quad (4)$$

where d_t is the treated film thickness, and N_p and N_{np} are the number of porous PAH/PAA and dense PAH/SPS blocks, respectively. Finally, the first-order reflected wavelength (λ_1) was obtained from reflectivity measurements on the film, and a previously reported value (1.55) of n_{np} was utilized,[46] allowing calculation of n_p by eq 3. Comparisons of simulations of the reflectivity curves with the experimental results were used to confirm the validity of the above assumptions and calculations. Theoretical reflectivity curves were calculated using the transfer matrix method as outlined earlier.

In the experiments on vapor detection, a cross-linked film was put into a closed quartz spectrophotometer cell with air inside. The cross-linking was performed by heating the film at 140 °C for 5 h.[47] The transmittance spectrum was obtained on a Cary 5E spectrophotometer. The film was then put into a closed quartz spectrophotometric cell with a saturated analyte vapor. The transmittance of the film was measured at the wavelength of the reflection band until it reached an asymptotic upper limit. The same film was used for all vapor-sensing experiments, but both the film and the spectrophotometric cell were dried in a vacuum before use with another analyte.

Results and Discussion

Fabrication of Nanoporous Heterostructures. Polyelectrolyte multilayers constructed from PAH and PAA can exhibit reversible, pH-driven morphological reorganizations leading to the formation of micro- and nanoporous films.[12,35] For example, multilayers assembled with the PAH dipping solution at a pH of 7.5 and the PAA dipping solution at a pH of 3.5 (7.5/3.5 PAH/PAA) form micropores after a brief exposure to a pH 2.4 aqueous solution,[35] while 8.5/3.5 PAH/PAA multilayers form nanopores after immersion in a pH 1.8 aqueous solution.[12] In both cases, a final brief rinse in water completes the porosity transformation. To date, all of this work has been carried out on thin films comprised only of the porosity forming PAH/PAA multilayers. It is of interest from both a fundamental and technological standpoint to determine whether these same morphological reorganizations can be induced in

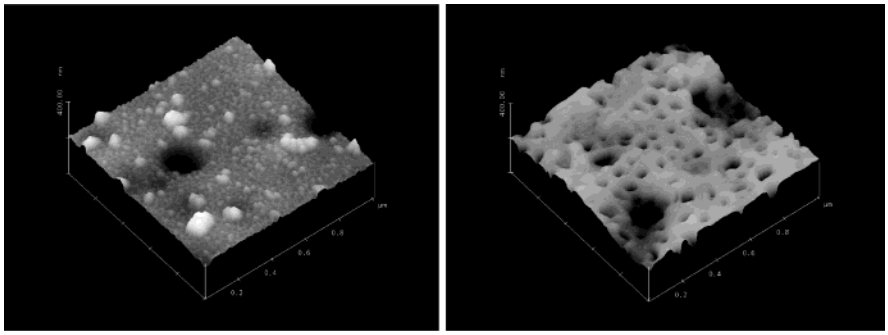

A B

Figure 1. AFM images of a $(PAH/PAA)_{8.5}-(PAH/SPS)_{25}$ film surface with a PAH/SPS block on the top of a porous PAH/PAA block (A) and a porous $(PAH/PAA)_{8.5}$ film (B) (*X*: 0.2 μm/div; *Z*: 200 nm/div).

confined geometries such as those found in more complex multilayer heterostructures. To accomplish this task, we fabricated multilayer heterostructures within which the porosity forming PAH/PAA bilayers were sandwiched between (or constrained by) nonporosity forming PAH/poly(sodium 4-styrenesulfonate) (SPS) bilayers.

In the first and simplest case, 8.5 bilayers of 8.5/3.5 PAH/PAA were surface capped with 25 bilayers of PAH/SPS ($(PAH/PAA)_{8.5}-(PAH/SPS)_{25}$). Ellipsometry measurements revealed that the PAH/PAA and PAH/SPS blocks in the fully dense structure were 86 and 47 nm thick, respectively, and the average refractive index of the film was 1.55. The first treatment evaluated was a 30 s immersion in a pH 1.8 acidic solution followed by a 15 s rinse in deionized water (pH 5.5), conditions previously found to create nanopores in 8.5/3.5 PAH/PAA multilayers. After the treatment, multiple macroscopic cracks were observed on the film surface most likely induced by an uncontrolled swelling of the underlying PAH/PAA block, which in turn generated fractures in the less swellable outermost PAH/SPS block. In contrast, no cracks were observed when a $(PAH/PAA)_{8.5}-(PAH/SPS)_{25}$ film was treated with a pH 2.2 acidic solution for 1 min followed by a 1 min rinse in deionized water. In this case, a more controlled swelling of the underlying PAH/PAA block eliminated the formation of cracks in the PAH/SPS surface block. After this treatment, the total dry film thickness increased from 133 to 230 nm while the average refractive index decreased from 1.55 to 1.38. During the fabrication process, the PAH/SPS block was assembled at pH 4.0 with both polymers in their fully ionized form. This bilayer system swells slightly in acidic solution and collapses back to its original thickness and refractive index (1.55) in the dry state.[46] Thus, the change in dry thickness observed after treatment is the result of a change in the PAH/PAA block. All of these observations suggest that the film thickness change is due to the formation of pores selectively in the PAH/PAA block.

The surface of the pH 2.2 treated $(PAH/PAA)_{8.5}-(PAH/SPS)_{25}$ film was examined using atomic force microscopy (AFM) (Figure 1A). The measured RMS surface roughness (14.2 nm) was lower than that of a porous 8.5-bilayer PAH/PAA film (rms roughness 23.5 nm) formed on a silicon wafer with the same treatment (Figure 1B), indicating that the presence of a PAH/SPS capping block results in a smoother surface after porosity development. Dimples on the order of a couple of hundred nanometers, however, were observed on the treated $(PAH/PAA)_{8.5}-(PAH/SPS)_{25}$ film. These craters resulted from the collapse of the PAH/SPS block over larger pores formed in the underlying PAH/PAA block. Large pores of similar dimension can be seen in the 8.5-bilayer PAH/PAA film after treatment (Figure 1B). As will be mentioned later, a small fraction of pores large enough to scatter light can be formed during the porosity inducing treatment. No dimples, however, were observed on the surface of a treated film capped with a thicker PAH/SPS block ($(PAH/PAA)_{8.5}-(PAH/SPS)_{50}$; thickness of PAH/SPS block: 112 nm). The rms surface roughness in this case is close to the roughness of a dense $(PAH/SPS)_{50}$ film, which was measured to be ca. 9 nm. To avoid the dimple effect, all multilayer films were subsequently constructed with PAH/SPS blocks comprised of 50 bilayers.

On the basis of the above results, it is clear that the pH of the porosity inducing treatment and the thickness of an adjacent nonporosity forming block can influence the properties and microstructure of the final multilayer film. Thus, the treatment needed to create nanopores within confined regions of a multilayer film must be optimized for the particular heterostructure under consideration. The basic goal is to avoid the formation of micropores and at the same time use conditions that do not destroy or disrupt the heterostructure organization by, for example, the effects of uncontrolled swelling. Factors such as (i) the number and sequence of PAH/PAA and PAH/SPS bilayers, (ii) the pH of the acid treatment solution, and (iii) the immersion time in the acid and rinse solutions are important parameters that need to be considered.

To explore a more complicated heterostructure, a series of films comprised of PAH/PAA bilayers (1−10 bilayers) sandwiched between two 50-bilayer PAH/SPS blocks were fabricated. Two different treatment solutions (pH 2.3 and pH 2.2) were used to induce porosity in the PAH/PAA regions. The sandwich structures—$(PAH/SPS)_{50}-(PAH/PAA)_m-(PAH/SPS)_{50}$ (m = 1, 1.5, 2, 2.5, 3, 3.5, 4, 4.5, 5, 5.5, 6, 7, 8, 9, 10)—were immersed in a pH 2.3 acidic solution for 1 min followed by a 1 min rinse in deionized water. The $(PAH/SPS)_{50}-(PAH/PAA)_{7-10}-(PAH/SPS)_{50}$ films turned cloudy after this treatment, suggesting that a high level of unwanted micropores was generated in heterostructures with the thickest PAH/PAA blocks (m = 7, 8, 9, 10). Heterostructures with fewer than seven PAH/PAA bilayers, on the other hand, were essentially transparent after treatment, indicating that physical constraints caused by the surrounding PAH/SPS blocks can influence the length scale of porosity development in the PAH/PAA layers. Without the PAH/SPS blocks, for example, PAH/PAA

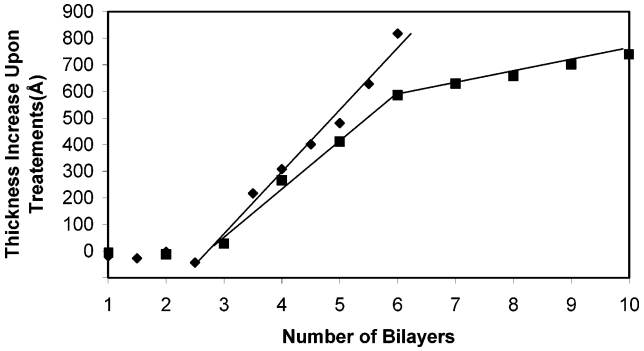

Figure 2. Thickness change of PAH/PAA blocks with different number of bilayers after low-pH treatment: ◆, $(PAH/SPS)_{50}-(PAH/PAA)_m-(PAH/SPS)_{50}$ (m = 1, 1.5, 2, 2.5, 3, 3.5, 4, 4.5, 5, 5.5, 6) films with pH 2.3 treatment; ■, $(PAH/SPS)_{50}-(PAH/PAA)_m-(PAH/SPS)_{50}$ (m = 1, 2, 3, 4, 5, 6, 7, 8, 9, 10) films with pH 2.2 treatment.

films with six bilayers would form micropores with this treatment.

Figure 2 (diamonds) shows the change in thickness of the PAH/PAA block induced by porosity treatment as a function of the number of PAH/PAA bilayers incorporated in the heterostructure (m = 1, 1.5, 2, 2.5, 3, 3.5, 4, 4.5, 5, 5.5, 6) as measured by profilometry. The thickness values were estimated with the assumption that the dry-state thickness of the PAH/SPS blocks is not influenced by the treatment (see Experimental Section). No change in thickness was observed for heterostructures containing 1−2.5 bilayers of PAH/PAA. Thereafter, the thickness change of the PAH/PAA block induced by treatment increases linearly with increasing number of PAH/PAA bilayers.

$(PAH/SPS)_{50}-(PAH/PAA)_m-(PAH/SPS)_{50}$ (m = 1, 2, 3, 4, 5, 6, 7, 8, 9, 10) films were also treated with a 1 min immersion in a pH 2.2 aqueous solution followed by a 1 min water rinse. In this case, all films remained clear after the treatment, suggesting that a stronger driving force for phase separation (due to a lower pH) produces a smaller fraction of micropores within the nanoporous structure.[12] The thickness change of the PAH/PAA blocks induced by this treatment is also presented in Figure 2 (squares). Again, it is observed that no thickness change takes place in heterostructures with 1−2 PAH/PAA bilayers. The thickness change then increases linearly with increasing number of deposited PAH/PAA bilayers up to six bilayers, at which point a slope change is observed reflecting a smaller thickness change increment. The smaller thickness increment observed in the 3−6 PAH/PAA bilayer range for the pH 2.2 treatment compared to the pH 2.3 treatment indicates that a lower level of porosity is developed in the former case; a conclusion confirmed by refractive index results to be discussed. We believe that the change in slope that occurs at six PAH/PAA bilayers in films treated at pH 2.2 is due to the fact that the 1 min treatment time is not sufficient to activate the full porosity transition in these thicker PAH/PAA blocks. To confirm this hypothesis, a $(PAH/PAA)_8-(PAH/SPS)_{50}$ multilayer film and a $(PAH/PAA)_8-(PAH/SPS)_{25}$ multilayer film were assembled onto silane-coated glass substrates. Both films were treated with a 1 min immersion in a pH 2.2 solution followed by a 1 min water rinse. The thickness of the $(PAH/PAA)_8-(PAH/SPS)_{25}$ film increased 80 nm with this treatment whereas the thickness of the $(PAH/PAA)_8-(PAH/SPS)_{50}$ film increased by only 66 nm. Thus, in the same period of time, the thicker PAH/SPS capping block presents a more effective barrier to the diffusion of the treatment solution. Longer treatment times produced a larger thickness change in the film with the thicker PAH/SPS block, but this occurred with the formation of light scattering micropores. Similar results were obtained if the thickness of the PAH/PAA block increased. This again reinforces the importance of optimizing treatment conditions to favor nanopore formation over micropore formation in PAH/PAA bilayers present in confined geometries. In general, as the thickness of the multilayer heterostructure increases, the porosity inducing treatment must be modified appropriately. As will be discussed, a multiple treatment protocol works best with very thick films.

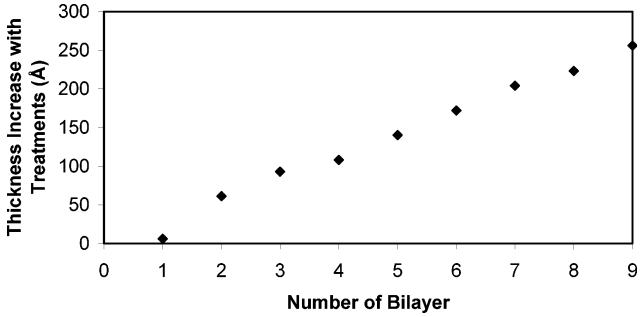

Figure 3. Thickness change of $(PAH/SPS)_{50}-(PAH/PAA)_{1-9}$ films with pH 1.8 treatment.

The fact that all multilayer heterostructures with 1−2.5 bilayers of PAH/PAA did not undergo the porosity transition indicates that interpenetration of the polymer chains nearest to the PAH/SPS blocks is preventing the phase separation process from taking place. It has now been well established that the polymer chains in polyelectrolyte multilayers are well interpenetrated.[48−50] Best estimates for PAH/PAA−PAH/SPS heterostructures are that a single polymer chain penetrates into 1−2 surrounding bilayers.[48] To estimate indirectly how much interpenetration occurred at the interface of a PAH/PAA and PAH/SPS block, the thickness change of a film comprised of 1−9 bilayers of PAH/PAA assembled onto a PAH/SPS block with 50 bilayers was examined by using profilometry and confirmed by ellipsometry. Thickness measurements were made after a 30 s immersion in a pH 1.8 solution followed by a 15 s water rinse. A pH 1.8 acidic solution was used to ensure that only nanopore formation occurred in the PAH/PAA bilayers. As shown in Figure 3, only a slight thickness change was detected for the film with one PAH/PAA bilayer deposited onto the PAH/SPS block. In films with from 2 to 9 bilayers of PAH/PAA, the thickness change observed increased linearly with increasing number of PAH/PAA bilayers. These results combined with the results obtained from sandwich structures indicate that chain interpenetration sufficient to modify physical properties occurs at the level of about 1−2 bilayers. Thus, for a PAH/PAA block sandwiched between two PAH/SPS blocks, the top and bottom 1−2 PAH/PAA bilayers adjacent to the PAH/SPS blocks are restricted from undergoing the porosity transition due to chain interpenetration.

Optical Properties of Nanoporous Heterostructures. The selective introduction of nanoporosity in multilayer heterostructures should lower the refractive index of the PAH/PAA regions. Reflectivity measurements coupled with suitable modeling can be used to

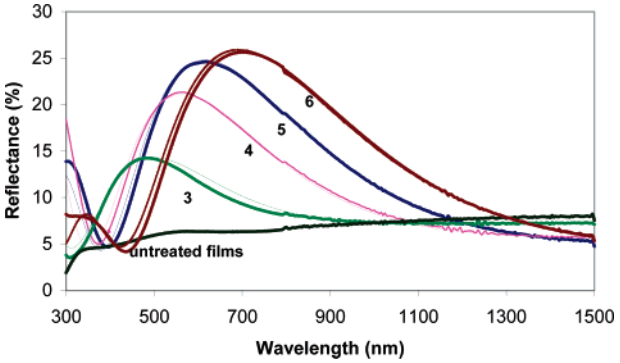

Figure 4. Reflectance of $(PAH/SPS)_{50}-(PAH/PAA)_m-(PAH/SPS)_{50}$ ($m = 3, 4, 5, 6$) films with pH 2.3 treatment. The thick line is experimental data, and the thin line is the simulation.

determine the refractive index of the porous PAH/PAA domains. A multiblock stack comprised of alternating regions of high and low refractive index is an example of a one-dimensional photonic structure (a Bragg reflector). With suitable block thicknesses, multilayer heterostructures of this type exhibit reflectivity bands in the visible region of the spectrum; i.e., they behave as dielectric mirrors. Their optical behavior depends on the refractive index and thickness of each block in the structure according to eq 3 (see Experimental Section). The average effective refractive index of the porous PAH/PAA blocks of each multilayer heterostructure was determined by inserting experimental data, including the first-order reflected wavelength of the film, the measured thickness and the known refractive index (1.55) of the PAH/SPS blocks,[46] and the measured thickness of the porous PAH/PAA block into eq 3. Further, a comparison of simulations of the reflectivity curves with the experimental results can be used to confirm the results of this calculation. Theoretical reflectivity curves were calculated using the transfer matrix method[43,44] (see Experimental Section for details).

Using this approach, the refractive index of the porous PAH/PAA block in $(PAH/SPS)_{50}-(PAH/PAA)_m-(PAH/SPS)_{50}$ heterostructure films with $m = 3$, 4, 5, and 6 was calculated to be 1.24, 1.19, 1.16, and 1.15, respectively (pH 2.3 treatment). Figure 4 shows a comparison of the measured reflectance of these films with the reflectance curves obtained by a simulation that uses the experimentally measured thicknesses of the PAH/PAA and PAH/SPS blocks, the known refractive index of a PAH/SPS multilayer film, and the above indicated refractive index values for the porous PAH/PAA block. As indicated in Figure 4, excellent agreement was obtained between experiment and simulation.

As the number of PAH/PAA bilayers increases, the peak of the reflectance band shifts to longer wavelengths and increases in intensity. The band shift is a result of the thickness increase and index change of the PAH/PAA blocks, whereas the intensity increase is due to a decrease in the refractive index of the PAH/PAA block. The fact that the apparent refractive index of the PAH/PAA block decreases with increasing number of bilayers is a consequence of the previously discussed layer interpenetration that occurs at the PAH/PAA−PAH/SPS interface. The estimated refractive index of the PAH/PAA block is an average of the refractive index of the nonporous, interpenetrated PAH/PAA bilayers and the porous PAH/PAA regions. The contribution of the nonporous bilayers to this average becomes less important as the total thickness of the PAH/PAA block increases. Given the fact that different treatments/structures may influence this interpenetration thickness value, all refractive index values for the porous PAH/PAA regions are reported in this paper as the effective values that include contributions from the nonporous interpenetrated interfacial regions and from the fully porous zones described above. (See the Appendix for an analysis of the interpenetration thickness and the refractive index of the porous PAH/PAA regions.)

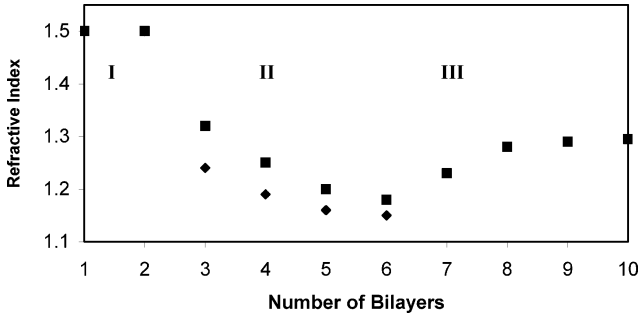

Figure 5. Refractive index of $(PAH/SPS)_{50}-(PAH/PAA)_m-(PAH/SPS)_{50}$ ($m = 1-10$) films with pH 2.2 treatment (■) and pH 2.3 treatment (◆).

Figure 5 presents refractive index data for the PAH/PAA block in $(PAH/SPS)_{50}-(PAH/PAA)_m-(PAH/SPS)_{50}$ films ($m = 1-6$) that were treated at pH 2.3 (diamonds) and the PAH/PAA block in $(PAH/SPS)_{50}-(PAH/PAA)_m-(PAH/SPS)_{50}$ films ($m = 1-10$) that were treated at pH 2.2 (squares). Refractive index values were obtained by putting experimental data in eq 3 and confirmed by the agreement between simulations and the measured reflectivity curves. These data show that the porosity inducing treatment at pH 2.3 produces a PAH/PAA block with a lower refractive index than the pH 2.2 treatment, confirming that a lower level of porosity is developed with the pH 2.2 treatment. As mentioned earlier, with this lower pH treatment, it is possible to add more PAH/PAA bilayers without the complication of excessive micropore formation. Three distinct regions can be identified in Figure 5. In region I (1−2 PAH/PAA bilayers), the refractive index does not change because the development of porosity is restricted due to interpenetration at the PAH/SPS interfaces. In region II (3−6 PAH/PAA bilayers), the average refractive index decreases with increasing PAH/PAA block thickness as the contribution to the index by the interpenetrated PAH/PAA layers decreases. In region III (7−10 PAH/PAA bilayers), the refractive index increases with increasing PAH/PAA block thickness. In this case, a longer diffusion and transition time would be required to achieve a lower index due to the thickness of the PAH/PAA block. The treatment times used in this experiment produce a lower level of pore formation within thick PAH/PAA blocks (7−10 bilayers) compared to thin PAH/PAA blocks (3−6 bilayers) and therefore result in a smaller drop in the refractive index with increasing number of bilayers. Recall that longer treatment times, however, can induce micropore formation.

Fabrication of Nanoporous Bragg Reflectors. Bragg reflectors have numerous applications in optical communication systems,[51,52] optical fiber sensing,[53,54] lasers,[55] and display devices.[56] Inorganic Bragg reflectors have been fabricated using porous silicon multilayers[57] and chemical vapor deposition (MOVCD) of different semiconductor materials.[58] Organic Bragg

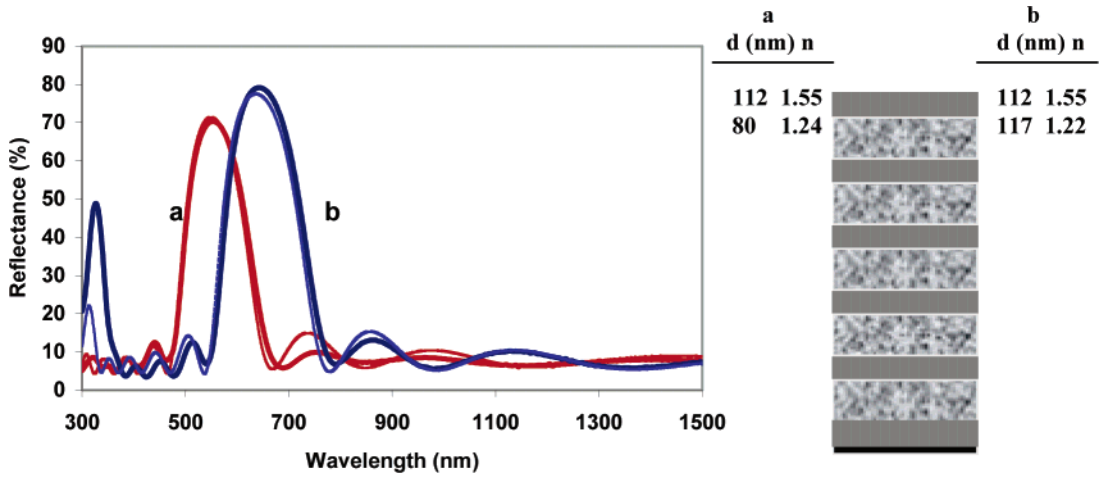

Figure 6. Reflectance and structures of a pH 2.3 treated $(PAH/SPS)_{50}-[(PAH/PAA)_4-(PAH/SPS)_{50}]_5$ film (a) and a pH 2.3 treated $(PAH/SPS)_{50}-[(PAH/PAA)_6-(PAH/SPS)_{50}]_5$ film (b). The thick line is experimental data, and the thin line is the simulation.

reflectors have been built using holographic polymer-dispersed liquid crystal (HPDLC)[59−62] techniques, block copolymers,[63] and polyelectrolyte multilayers.[39,64] In our case, the ability to introduce nanoporosity controllably in select regions of a multilayer heterostructure makes it possible to design and fabricate conformable Bragg reflectors with any desired optical profile over a wide range of the electromagnetic spectrum. When considering the fabrication of multilayer heterostructures containing multiple alternating porous and nonporous regions, the issue of treatment pH and time becomes particularly important. For example, we fabricated a multilayer heterostructure with five alternating heterostructure regions containing the following sequence: $(PAH/SPS)_{50}-[(PAH/PAA)_6-(PAH/SPS)_{50}]_5$. In this film, the thicknesses of the PAH/SPS and PAH/PAA blocks before porosity treatment were 112 and 61 nm, respectively. The porosity forming treatment involved immersing the film in a pH 2.3 solution for 3 min, drying it with air, rinsing it with water for 3 min, and then drying the film again. Because of the significant total film thickness, this two-step porosity formation treatment cycle was repeated three times. The final thickness of the treated film was 1257 nm. As mentioned previously, the PAH/SPS blocks do not change in thickness after the porosity forming treatment; the thickness and refractive index remain at 112 nm and 1.55, respectively. Assuming a complete and uniform transformation of the PAH/PAA regions to the nanoporous state, the average thickness of these regions was estimated to be to 117 nm using eq 4 (see Experimental Section).

Figure 6b shows the experimental reflectance spectrum of this dielectric mirror as well as the theoretical reflectance spectrum calculated by using the measured thickness (112 nm) and refractive index of the PAH/SPS blocks (1.55) and calculated index of the porous PAH/PAA blocks (1.22, calculated using eq 3) and the above-indicated average thickness value (117 nm) for the porous PAH/PAA blocks. The simulation predicts the existence of a reflection peak at 633 nm and a maximum reflectivity of 79%. Both are in excellent agreement with the experimental results, demonstrating that, with suitable treatment, dielectric mirrors with predictable optical properties can be designed and fabricated. The good agreement between the experimental data and the theoretically predicted reflectivity also suggests that each PAH/PAA region is uniformly converted into a similar state of nanoporosity (i.e., same refractive index and thickness).

A clear advantage of the layer-by-layer processing technique is that it is possible to easily control the thickness and sequence of the various blocks present in a dielectric mirror by simply controlling the number and types of layers deposited during assembly.[39] This means that the position and intensity of the reflectance band (or bands) of the dielectric mirror are readily tunable.

Figure 6a shows the reflectance curve of a dielectric stack fabricated with five PAH/PAA blocks containing fewer PAH/PAA bilayers: $(PAH/SPS)_{50}-[(PAH/PAA)_4-(PAH/SPS)_{50}]_5$. In this case, the as-assembled thicknesses of the PAH/SPS and PAH/PAA blocks were 112 and 38 nm, respectively. Using the porosity treatment outlined above, the thickness of the PAH/PAA blocks increased to 80 nm and the refractive index was calculated to be 1.24 using eq 3. The simulation of this dielectric mirror is again in good agreement with the experimental results: both of which show the expected shift of the reflectance peak to lower wavelength (545 nm vs 633 nm). The effective medium approximation (eqs 1 and 2, see Experimental Section) was also used to calculate the refractive index of the porous PAH/PAA blocks in the above dielectric mirrors and predicted similar index values within 5% (results: $n = 1.28$ for the 6-bilayer PAH/PAA block and $n = 1.26$ for the 4-bilayer PAH/PAA block).

Figure 7 shows reflectance data for a multilayer dielectric mirror with a maximum reflectance of more than 90% at 605 nm. The structure of this multilayer, $(PAH/SPS)_{50}-[(PAH/PAA)_6-(PAH/SPS)_{50}]_{11}-(PAH/SPS)_{50}$, contains 11 distinct 6-bilayer PAH/PAA blocks and a total of 1432 individually adsorbed polymer layers. To generate comparable levels of nanoporosity in all of the PAH/PAA regions within this very thick film (as assembled thickness more than 2.4 μm), it was necessary to first assemble about half of the structure (i.e., six alternating PAH/PAA−PAH/SPS blocks) and then induce nanoporosity in the PAH/PAA regions. The film was then thermally cross-linked (5 h at 140 °C) to prevent further porosity development followed by addition of the remaining PAH/PAA−PAH/SPS layers needed to complete the structure. The porosity inducing treatment in both cases involved immersion in a pH 2.3 solution for 3 min followed by a 3 min immersion in deionized water. This process was repeated three times.

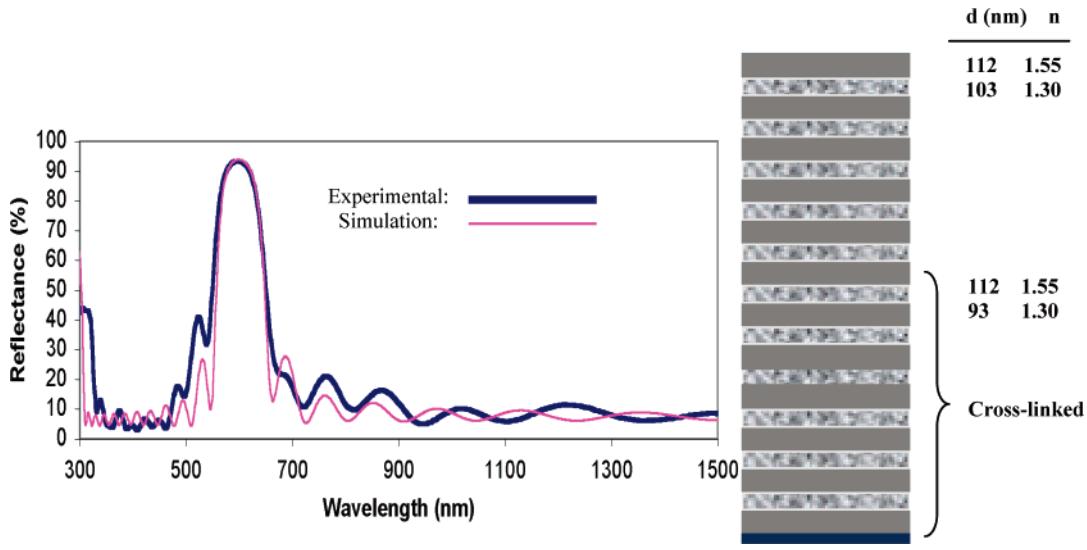

Figure 7. Reflectance and structure of a treated $(PAH/SPS)_{50}-[(PAH/PAA)_{11}-(PAH/SPS)_{50}]_6-(PAH/SPS)_{50}$ film.

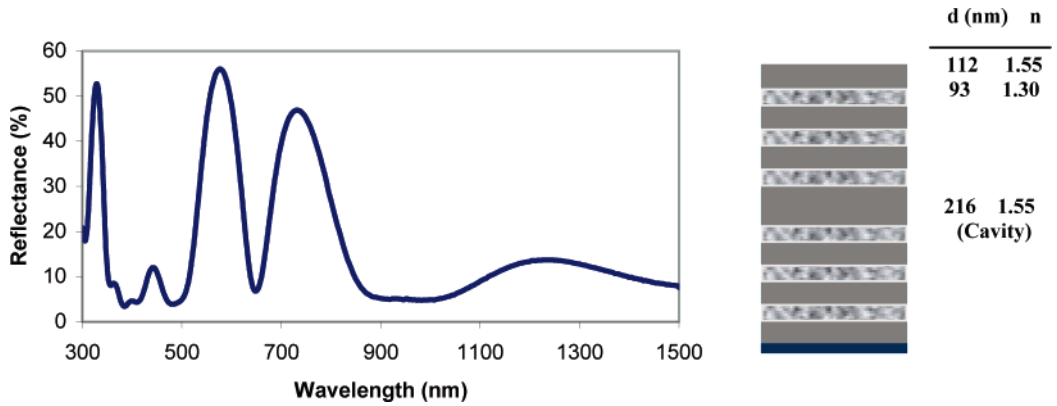

Figure 8. A Fabry−Perot optical cavity based on a $(PAH/SPS)_{50}-[(PAH/PAA)_6-(PAH/SPS)_{50}]_2-(PAH/PAA)_6-(PAH/SPS)_{100}-(PAH/PAA)_6-[(PAH/SPS)_{50}-(PAH/PAA)_6]_2-(PAH/SPS)_{50}$ assembly.

Because of cross-linking induced shrinkage, the thickness of the top five PAH/PAA blocks is about 10% larger than that of the six PAH/PAA blocks assembled in the first stage of this process. When this is taken into account, the simulation of this structure produces a reflectivity spectrum that nicely matches the experimental results (Figure 7), demonstrating the remarkable control possible over optical properties even with exceptionally thick films.

To demonstrate the fabrication of a more complex dielectric mirror, we created a multilayer heterostructure with a Fabry−Perot optical cavity.[34,65] The presence of such a cavity, created by producing a thicker PAH/SPS block in the center of the film, opens up a transmission window in the reflectivity band. The structure of this film is shown in Figure 8 along with its measured reflectivity curve. The film contained the following layer arrangement: $(PAH/SPS)_{50}-[(PAH/PAA)_6-(PAH/SPS)_{50}]_2-(PAH/PAA)_6-(PAH/SPS)_{100}-(PAH/PAA)_6-[(PAH/SPS)_{50}-(PAH/PAA)_6]_2-(PAH/SPS)_{50}$. The nanoporosity was created by using three cycles of a 3 min immersion in a pH 2.3 solution followed by a 3 min immersion in deionized water. The 216 nm PAH/SPS optical cavity in this structure opens up a transmission window at 649 nm, a wavelength about twice the equivalent optical thickness of the PAH/SPS block.

Reversible pH-Gated Nanoporosity Transitions. We have previously reported that the nanoporosity transitions in 8.5/3.5 PAH/PAA multilayers are reversible.[12] To determine whether pH-gated reversible nanoporosity transitions are possible within confined PAH/PAA mutlilayers, we fabricated a multilayer heterostructure with five PAH/PAA blocks: $[(PAH/PAA)_6-(PAH/SPS)_{50}]_5$. The nanoporosity was created by using three cycles of a 3 min immersion in a pH 2.3 solution followed by a 3 min immersion in deionized water with air-drying between each step. To examine the ability to open and close pores reversibly, the heterostructure was alternately immersed for 3 min in pH 2.3 and pH 5.5 solutions, and the dry-state film thickness after each treatment was examined by profilometry. As shown in the inset of Figure 9, the dry thickness of this film changed reversibly from 900 to 1180 nm, suggesting a reversible change in the thickness of the PAH/PAA blocks. The reflectivity data shown in Figure 9 confirm that the origin of this reversible thickness change is the opening and closing of nanopores in the PAH/PAA blocks. While three cycles of the two-step treatment are required to induce nanopores in the PAH/PAA regions, only a single subsequent 3 min immersion in the pH 5.5 or 2.3 solution is needed to reversibly open or close these nanopores. We believe that such behavior is observed because the initial transition involves a phase separation process, which requires multiple treatments, whereas the opening and closing of pores occurs within the new structure created by the phase separation process, which can be accomplished by a single treat-

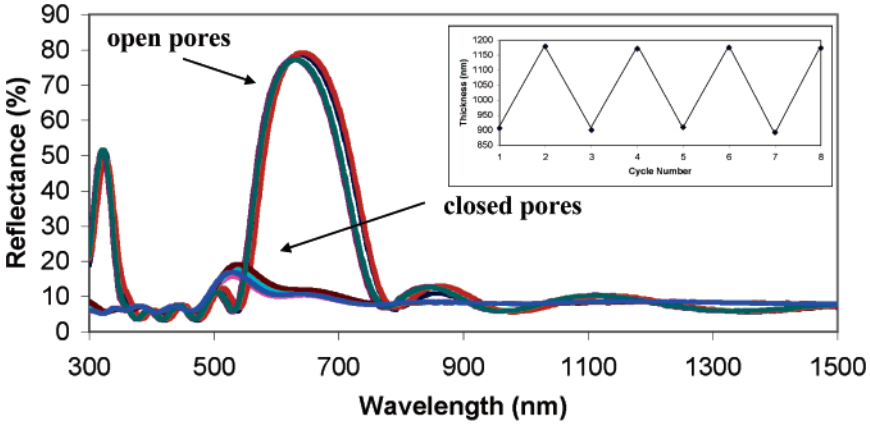

Figure 9. Reversible pH-gated porosity transitions of a $[(PAH/PAA)_6-(PAH/SPS)_{50}]_5$ film. Inset shows the reversible change of the film thickness. Data for cycles 1, 3, 5, and 7 were obtained after the film was immersed into a pH 2.3 solution for 3 min and subsequently dried in air. The data for cycles 2, 4, 6, and 8 were obtained after a 3 min immersion in deionized water.

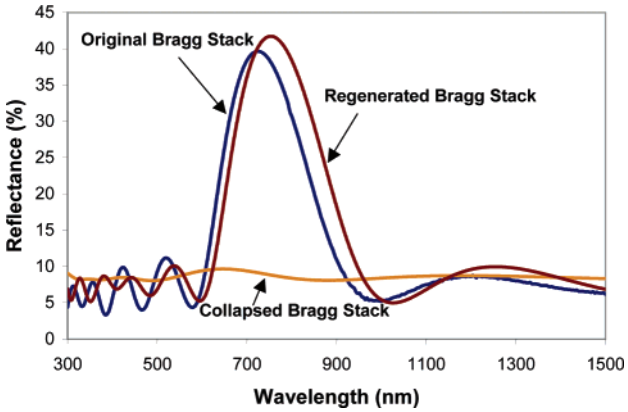

Figure 10. Bragg stack of a $[(PAA/PAH)_8-(PAH/SPS)_{50}]_3$ film before and after regeneration process.

ment. In the open pore state, the film exhibits a reflectivity band with a wavelength maximum of 639 nm, whereas in the closed pore state, the film exhibits the reflection behavior close to the as-assembled, nonporous film. (After pore closing, a small amount of index contrast remains between the PAH/PAA and PAH/SPS blocks (about 0.05).) The position and intensity of the reflectivity band observed in the open pore state indicate that the PAH/PAA regions are nanoporous with an effective refractive index of 1.23.

The PAH/PAA regions of these multilayer heterostructures can be cycled repeatedly between the open and closed pore state by these very simple pH treatments. (Recycling can be performed at least 5 times with consistent results; deviations are < 5%.) If a nanoporous film is immersed in deionized water overnight, however, the nanopores are eliminated due to a further reorganization of the polymer chains. We observed similar behavior with both microporous[35] and nanoporous multilayers of PAH/PAA.[12] The mechanism of this long-time rearrangement is still under investigation. It is possible, however, to regenerate the nanoporous regions by treatment in a low-pH solution. For example, Figure 10 shows the reflectivity curves of a $[(PAH/PAA)_8-(PAH/SPS)_{50}]_3$ dielectric mirror (1) after the overnight treatment in water and (2) after a pH 2.2 treatment and subsequent water rinse. The overnight water treatment eliminates the Bragg reflection, but the reflection band is observed to reemerge after the low-pH treatment. The reflectance band of the regenerated Bragg stack displays a slightly higher reflectance and a small shift to the red, most likely due to an additional expansion of the PAH/PAA blocks.

Applications of Nanoporous Bragg Reflectors. It is clear that the optical properties of dielectric mirrors that utilize nanoporosity transitions to create the low index blocks of a Bragg stack are highly sensitive to changes in the level of porosity. In addition, any substance that penetrates into the pores would be expected to modify the refractive index of these regions and hence the optical properties. This strong coupling between optical properties and the physical/chemical state of the nanoporous regions opens up numerous possibilities in applications ranging from vapor sensors to monitorable drug delivery systems to switchable Bragg gratings.[61,66] In the vapor sensing area, various kinds of Bragg stacks have been investigated. Bragg stacks based on polymer replicas of nanoporous silicon films,[33] for example, exhibit a significant reflectance band shift upon exposure to various solvent vapors. The shift is caused by the condensation of analyte vapors within pores and the concomitant change in the refractive index of the porous regions.[67]

To demonstrate this effect with our Bragg reflectors, we built a $[(PAH/PAA)_8-(PAH/SPS)_{50}]_9$ film and converted it to the nanoporous state by alternating immersion for 2 min in a pH 2.2 and pH 9.5 solution. In this case a higher pH rinsing solution was used to enhance nanopore formation in the thick PAH/PAA blocks. The film was then cross-linked by heating at 140 °C for 5 h to stabilize the structure against possible rearrangement during solvent exposure.[47] The transmittance spectrum of this film is presented in Figure 11. The transmittance spectrum of the film in air exhibits a trend of decreasing transmission with decreasing wavelength due to the presence, in the PAH/PAA regions, of micron-sized pores that scatter light. Upon exposure to a saturated vapor either of water, ethanol, acetone, or toluene, the reflectivity band decreases in intensity and shifts to longer wavelengths, leading to an increase in transmittance and a shifting of the minimum transmittance wavelength. The light scattering caused by the larger pores also diminished upon exposure of the film to these vapors. In these experiments, the same film was used for each solvent. Between experiments the solvent was removed by air- or vacuum-drying, during which the refractive index of the porous regions returned to the original value as the condensed analyte liquid evaporated from the pores. The transmittance spectrum of the dried film always returned to curve 1

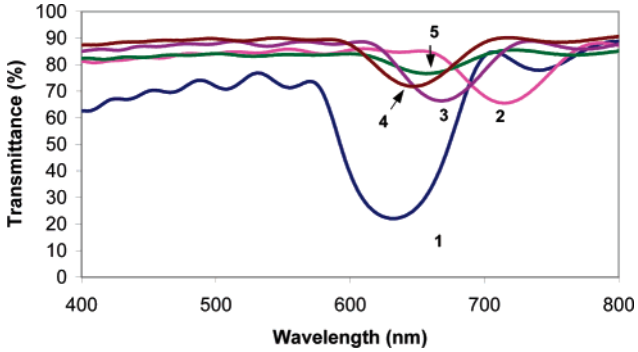

Figure 11. Transmittance spectra of a treated $[(PAH/PAA)_8-(PAH/SPS)_{50}]_9$ film in air (1) and after exposure to water (2), ethanol (3), acetone (4), and toluene (5) vapors.

Table 1. Comparison of Different Analytes Applied in Vapor Sensor

vapor	air	water	ethanol	acetone	toluene
refractive index (20 °C)	1.00	1.33	1.36	1.39	1.49
peak transmittance (%)	22	66	67	72	77
peak wavelength (nm)	626	709	668	647	658

shown in Figure 11. These dramatic and reversible effects are a result of the change of the refractive indices of the nanoporous regions that occurs when they are penetrated by condensing solvent vapor.

A consideration of the refractive index of each liquid analyte provides insight into the mechanism behind these optical changes. In Table 1, along with the refractive index of each liquid analyte, we list the transmission level and wavelength of minimum transmission resulting from exposure to each solvent. The transmittance is higher when the film is exposed to the vapor of a material with a higher refractive index. The better refractive index match between the pores filled with analyte liquid and the polymer matrix results in a lower film reflectance, leading to a higher transmittance. The distinct optical changes observed with different vapors could be used to distinguish a specific analyte. Using the data generated from the toluene exposed film, it was possible to confirm that the solvent vapor was in fact condensing into the pores. The refractive index of PAH/PAA regions with toluene filled nanopores was calculated to be 1.50 using the effective medium approximation (eqs 1 and 2). Using this value in a reflectance simulation predicts a minimum transmission (76%) at 663 nm, which is in good agreement with the experimental result (77% at 658 nm). The more dramatic shift to the red observed with water (and somewhat with ethanol) most likely is due to a swelling of the multilayer by these more polar solvents.

Another intriguing possibility is the idea of filling the pores with drug molecules or electrically responsive molecules. In the former case, changes in the optical properties of the dielectric mirror can be used to monitor the loading and/or release of biomaterials such as DNA or drugs, an application that has been demonstrated in porous silicon-based reflectors.[68,69] Using multilayers, the rate of release of a drug through the heterostructure could be controlled by the choice of barrier layers and their thicknesses and sequence in the heterostructure. Liquid crystals, when loaded into the pores, can provide a means to vary the refractive index of the porous PAH/PAA blocks with application of an electric field, thereby producing a dynamically tunable Bragg reflector. Both of these applications are now being explored in our laboratory.

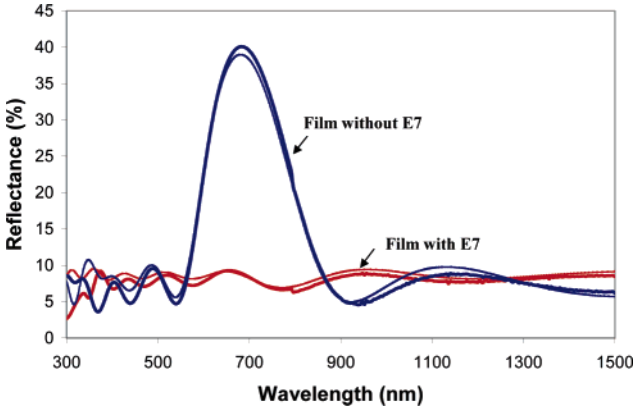

Figure 12. Reflectance of a cross-linked $[(PAH/PAA)_8-(PAH/SPS)_{50}]_3$ film infiltrated with E7 liquid crystals. The thick line is experimental data, and the thin line is the simulation.

To demonstrate that nonionic small molecules can in fact be loaded into the nanoporous regions of multilayer dielectric mirrors, we utilized the well-known liquid crystal E7. To accomplish this, the bottom portion of a thermally cross-linked multilayer heterostructure with nanoporous PAH/PAA blocks ($[(PAH/PAA)_8-(PAH/SPS)_{50}]_3$) was immersed into the liquid crystal. After a short period of time, the liquid crystal was observed to infiltrate the pores by a wicking effect. This process could be easily monitored by observing the film under a UV lamp. As the fluorescent liquid crystal wicked into the multilayer film, the film became fluorescent. The reflectivity of the film also changed dramatically as the liquid crystal filled the pores and modified the refractive index of the PAH/PAA regions. Figure 12 shows the change in reflectivity that occurs after the loading process. Before loading, the film behaves as a dielectric mirror with a reflectivity band centered at about 690 nm. This reflectivity band disappears when the liquid crystal is loaded into the pores.

The above results can be rationalized in following manner. The average/isotropic refractive index of the liquid crystal is 1.62. The average refractive index of the PAH/PAA regions therefore increases when the pores are filled, thereby reducing the index contrast between the PAH/PAA and PAH/SPS regions. The refractive index of E7 filled PAH/PAA blocks was calculated to be 1.57 using the effective medium approximation (eqs 1 and 2), and a theoretical simulation of the reflectivity curve of the E7 loaded film (see Figure 12) also suggests a refractive index of 1.57. The original reflectivity band was reestablished when the E7 molecules were extracted from the multilayer film using acetone. All of these observations coupled with the excellent agreement between the experimental and theoretical results support the notion that the liquid crystal molecules are uniformly loading the nanopores of the PAH/PAA regions.

These results show that nanoporous multilayer films can be used as vehicles for loading and releasing nonionic organic molecules. Preliminary results indicate that a variety of small molecules, drug and nondrug types, can be controllably manipulated in this manner. The use of these films in drug release applications as well as electrically switchable Bragg gratings is currently under investigation.

Acknowledgment. This work was supported in part by the DARPA BOSS Program and the MRSEC Pro-

gram of the National Science Foundation under Award DMR 02-13282. This work also made use of the Shared CMSE Experimental Facilities supported in part by the MRSEC Program of the National Science Foundation under Award DMR 02-13282.

Appendix

As mentioned in the paper, the interpenetration thickness at the PAH/SPS and PAH/PAA interface has been estimated using different methods.[48,49] The combination of experimental data and theoretical simulations of the sandwich structures of Figure 4 ((PAH/SPS)$_{50}$−(PAH/PAA)$_{3-6}$−(PAH/SPS)$_{50}$)) can also be used to estimate the interpenetration thickness as well as the actual refractive index of the porous PAH/PAA regions. Since the interpenetration region does not undergo porosity transitions with treatment, it can be considered as a solid polymeric region extending the PAH/SPS blocks. To estimate the "real" thickness of the solid and porous regions, we assumed an intermediate interpenetration thickness value from previously reported estimates.[48,49] This thickness was added at each interface between the PAH/SPS and PAH/PAA regions and subtracted from the porous PAH/PAA region. Optical simulations on the four sandwich structures (Figure 4) were then carried out, and the interpenetration thickness was systematically varied to obtain the closest match to the experimental data. The refractive index of the porous region was then estimated using eq 3. Using this approach, the two unknown parameters were determined; best fits were obtained when the refractive index of the porous PAH/PAA region was $n_p = 1.16 \pm 0.01$ and the interpenetration thickness was 4 nm. That is, a zone of thickness 4 nm at the top and bottom of each PAH/PAA region was restricted from participating in the porosity transition owing to its interpenetration with the fully dense PAH/SPS blocks on either side. This result shows that the level of porosity created in the porous PAH/PAA region that is about the same regardless of the number of deposited bilayers.

References and Notes

(1) He, T.; Mulder, M. H. V.; Wessling, M. *J. Appl. Polym. Sci.* **2003**, *87*, 2151.
(2) Peterson, D. S.; Rohr, T.; Svec, F.; Frechet, J. M. J. *Anal. Chem.* **2003**, *75*, 5328.
(3) Ling, F. H.; Lu, V.; Svec, F.; Frechet, J. M. J. *J. Org. Chem.* **2002**, *67*, 1993.
(4) Lakshmi, B. B.; Martin, C. R. *Nature (London)* **1997**, *388*, 758.
(5) Gu, W.; Zhou, W.-J.; Gin, D. L. *Chem. Mater.* **2001**, *13*, 1949.
(6) Deng, H.; Gin, D. L.; Smith, R. C. *J. Am. Chem. Soc.* **1998**, *120*, 3522.
(7) Chen, Y.; Ford, W. T.; Materer, N. F.; Teeters, D. *J. Am. Chem. Soc.* **2000**, *122*, 10472.
(8) Deleuze, H.; Schultze, X.; Sherrington, D. C. *Polymer* **1998**, *39*, 6109.
(9) Sundell, M. J.; Pajunen, E. O.; Hormi, O. E. O.; Nasman, J. H. *Chem. Mater.* **1993**, *5*, 372.
(10) Ruckenstein, E.; Hong, L. *Chem. Mater.* **1992**, *4*, 122.
(11) Walheim, S.; Schäffer, E.; Jürgen, M.; Setiner, U. *Science* **1999**, *283*, 520.
(12) Hiller, J.; Mendelsohn, J. D.; Rubner, M. F. *Nature Mater.* **2002**, *11*, 59.
(13) Adiga, S. P.; Brenner, D. W. *Nano Lett.* **2002**, *2*, 567.
(14) Jang, J.-H.; Shea, L. D. *J. Controlled Release* **2003**, *86*, 157.
(15) Sohier, J.; Haan, R. E.; de Groot, K.; Bezemer, J. M. *J. Controlled Release* **2003**, *87*, 57.
(16) Yang, F.; Murugan, R.; Ramakrishna, S.; Wang, X.; Ma, Y.-X.; Wang, S. *Biomaterials* **2004**, *25*, 1891.
(17) Shastri, V. P.; Hildgen, P.; Langer, R. *Biomaterials* **2003**, *24*, 3133.
(18) Lin, A. S. P.; Barrows, T. H.; Cartmell, S. H.; Guldberg, R. E. *Biomaterials* **2003**, *24*, 481.
(19) Misner, M. J.; Skaff, H.; Emrick, T.; Russell, T. P. *Adv. Mater.* **2003**, *15*, 221.
(20) Ulrich, R.; Du Chesne, A.; Templin, M.; Wiesner, U. *Adv. Mater.* **1999**, *11*, 141.
(21) Yi, D. K.; Kim, D.-Y. *Nano Lett.* **2003**, *3*, 207.
(22) Jiang, P.; Bertone, J. F.; Colvin, V. L. *Science* **2001**, *291*, 453.
(23) Zhang, G.; Fu, N.; Zhang, H.; Wang, J.; Hou, X.; Yang, B.; Shen, J.; Li, Y.; Jiang, L. *Langmuir* **2003**, *19*, 2434.
(24) Lin, Z.; Kim, D. H.; Wu, X.; Boosahda, L.; Stone, D.; LaRose, L.; Russell, T. P. *Adv. Mater.* **2002**, *14*, 1373.
(25) Kiefer, J.; Hilborn, J. G.; Manson, J. A. E.; Leterrier, Y.; Hedrick, J. L. *Macromolecules* **1996**, *29*, 4158.
(26) Zalusky, A. S.; Olayo-Valles, R.; Wolf, J. H.; Hillmye, M. C. *J. Am. Chem. Soc.* **2002**, *124*, 12761.
(27) Urbas, A. M.; Maldovan, M.; DeRege, P.; Thomas, E. L. *Adv. Mater.* **2002**, *14*, 1850.
(28) Xu, T.; Kim, H.-C.; DeRouchey, J.; Seney, C.; Levesque, C.; Martin, P.; Stafford, C. M.; Russell, T. P. *Polymer* **2001**, *42*, 9091.
(29) Takeoka, Y.; Watanabe, M. *Langmuir* **2002**, *18*, 5977.
(30) Park, S. H.; Xia, Y. *Adv. Mater.* **1998**, *10*, 1045.
(31) Jiang, P.; Hwang, K. S.; Mittleman, D. M.; Bertone, J. F.; Colvin, V. L. *J. Am. Chem. Soc.* **1999**, *121*, 11630.
(32) Holtz, J. H.; Asher, S. A. *Nature (London)* **1997**, *389*, 829.
(33) Li, Y. Y.; Cunin, F.; Link, J. R.; Gao, T.; Betts, R. E.; Reiver, S. H.; Chin, V.; Bhatia, S. N.; Sailor, M. J. *Science* **2003**, *229*, 2045.
(34) Yariv, A. *An Introduction to Theory and Applications of Quantum Mechanics*; Wiley: New York, 1982.
(35) Mendelsohn, J. D.; Barrett, C. J.; Chan, V. V.; Pal, A. J.; Mayes, A. M.; Rubner, M. F. *Langmuir* **2000**, *16*, 5017.
(36) Kim, B. Y.; Bruening, M. L. *Langmuir* **2003**, *19*, 94.
(37) Fu, Y.; Bai, S.; Cui, S.; Qui, D.; Wang, Z.; Zhang, X. *Macromolecules* **2002**, *35*, 9451.
(38) Fery, A.; Schloer, B.; Cassagneau, T.; Caruso, F. *Langmuir* **2001**, *17*, 3779.
(39) Wang, T. C.; Cohen, R. E.; Rubner, M. F. *Adv. Mater.* **2002**, *14*, 1534.
(40) Shiratori, S. S.; Rubner, M. F. *Macromolecules* **2000**, *33*, 4213.
(41) Romanov, S. G.; Maka, T.; Sotomayor Torres, C. M. *Phys. Rev. E* **1999**, *63*, 056603.
(42) Sareni, B.; Krahenbuhl, L.; Beroual, A.; Brosseau, C. *J. Appl. Phys.* **1996**, *80*, 1688.
(43) Abeles, F. *Ann. Phys.* **1950**, *5*, 596.
(44) Hecht, E. *Optics*, 4th ed.; Pearson Addison-Wesley: Reading, MA, 2001.
(45) Alfrey, T., Jr.; Gurnee, E. F.; Schrenk, W. J. *Polym. Eng. Sci.* **1969**, *9*, 400.
(46) Hiller, J. Ph.D. Thesis, Massachusetts Institute of Technology, 2003.
(47) Dai, J.; Jensen, A. W.; Mohanty, D. K.; Erndt, J.; Bruening, M. L. *Langmuir* **2001**, *17*, 931.
(48) Baur, J. W.; Rubner, M. F.; Reynolds, J. R.; Kim, S. *Langmuir* **1999**, *15*, 6460.
(49) Joly, S.; Kane, R.; Radzilowski, L.; Wang, T.; Wu, A.; Cohen, R. E.; Thomas, E. L.; Rubner, M. F. *Langmuir* **2000**, *16*, 1354.
(50) Decher, G. *Science* **1997**, *277*, 1232.
(51) Hill, K. O.; Fujii, Y.; Johnson, D. C.; Kawasaki, B. S. *Appl. Phys. Lett.* **1978**, *32*, 647.
(52) Dyer, P. E.; Farley, R. J.; Giedl, R.; Byron, K. C.; Reid, D. *Electron. Lett.* **1994**, *30*, 860.
(53) Liu, H. B.; Liu, H. Y.; Peng, G. D.; Chu, P. L. *Opt. Commun.* **2003**, *219*, 139.
(54) Kronenberg, P.; Rastogi, P. K.; Giaccari, P.; Limberger, H. G. *Opt. Lett.* **2002**, *27*, 1385.
(55) Woldeyohannes, M.; John, S. *J. Opt. B: Quantum Semiclass. Opt.* **2003**, *5*, R43.
(56) Pikas, D. J.; Kirkpatrick, S. M.; Tomlin, D. W.; Natarajan, L.; Tondiglia, V.; Bunning, T. J. *Appl. Phys. A* **2002**, *74*, 767.
(57) Vincent, G. *Appl. Phys. Lett.* **1994**, *64*, 2367.
(58) Egawa, T.; Jimbo, T.; Umeno, M. *J. Appl. Phys.* **1995**, *77*, 3836.
(59) Sutherland, R. L.; Natarajan, L. V.; Tondiglia, V. P.; Bunning, T. J. *Chem. Mater.* **1993**, *5*, 1533.
(60) Sutherland, R. L.; Tondiglia, V. P.; Natarajan, L. V.; Bunning, T. J.; Adams, W. W. *Appl. Phys. Lett.* **1994**, *64*, 1074.
(61) Crawford, G. P. *Opt. Photon. News* **2003**, 54.
(62) Jakubiak, T.; Bunning, T. J.; Vaia, R. A.; Natarajan, L. V.; Tondiglia, V. P. *Adv. Mater.* **2003**, *15*, 241.
(63) Edrington, A. C.; Urbas, A. M.; DeRege, P.; Chen, C. X.; Swager, T. M.; Hadjichristidis, N.; Xenidou, M.; Fetters, L.

J.; Joannopoulos, J. D.; Fink, Y.; Thomas, E. L. *Adv. Mater.* **2001**, *13*, 421.
(64) Nolte, A. J.; Rubner, M. F.; Cohen, R. E. *Langmuir* **2004**, *20*, 3304.
(65) Dirr, S.; Wiese, S.; Johannes, H.-H.; Kowalsky, W. *Adv. Mater.* **1998**, *10*, 167.
(66) Pikas, D. J.; Kirkpatrick, S. M.; Tomlin, D. W.; Natarajan, L.; Tondiglia, V.; Bunning, T. J. *Appl. Phys. A* **2002**, *74*, 767.
(67) Gao, J.; Gao, T.; Li, Y. Y.; Sailor, M. J. *Langmuir* **2002**, *18*, 2229.
(68) Chan, S.; Li, Y.; Rothberg, L. J.; Miller, B. L.; Fauchet, P. M. *Mater. Sci. Eng., C* **2001**, *15*, 277.
(69) Lin, V. S.-Y.; Motesharei, K.; Dancil, K.-P. S.; Sailor, M. J.; Ghadiri, M. R. *Science* **1997**, *278*, 840.

MA049593E